ARTICLE IN PRESS
+ MODEL
Available online at www.sciencedirect.com
ScienceDirect
ELSEVIER
Journal of Human Evolution xx (2007) 1–13
JHE

Biomechanics of phalangeal curvature

Brian G. Richmond [a,b,*]

[a] Center for the Advanced Study of Hominid Paleobiology, The George Washington University
[b] Human Origins Program, National Museum of Natural History, Smithsonian Institution

Received 20 November 2006; accepted 13 May 2007

Abstract

Phalangeal curvature has been widely cited in primate functional morphology and is one of the key traits in the ongoing debate about whether the locomotion of early hominins included a significant degree of arboreality. This study examines the biomechanics of phalangeal curvature using data on hand posture, muscle recruitment, and anatomical moment arms to develop a finite element (FE) model of a siamang manual proximal phalanx during suspensory grasping. Strain patterns from experiments on intact cadaver forelimbs validated the model. The strain distribution in the curved siamang phalanx FE model was compared to that in a mathematically straight rendition in order to test the hypotheses that curvature: 1) reduces strain and 2) results in lower bending strains but relatively higher compression.

In the suspensory posture, joint reaction forces load the articular ends of the phalanx in compression and dorsally, while muscle forces acting through the flexor sheath pull the mid-shaft palmarly. These forces compress the phalanx dorsally and tense it palmarly, effectively bending it 'open.' Strains in the curved model were roughly half that of the straight model despite equivalent lengths, areas, mechanical properties, and loading conditions in the two models. The curved model also experienced a higher ratio of compressive to tensile strains. Curvature reduces strains during grasping hand postures because the curved bone is more closely aligned with the joint reaction forces. Therefore, phalangeal curvature reduces the strains associated with arboreal, and especially suspensory, activity involving flexed digits. These results offer a biomechanical explanation for the observed association between phalangeal curvature and arboreality.

Keywords: Finite element analysis; Siamang; *Hylobates syndactylus*; Hand; Primate anatomy; Functional morphology; Bone curvature

Introduction

Phalangeal curvature is a widely discussed feature in primate functional morphology and paleontology. The association between dorsoventral curvature and the use of hands and feet on arboreal supports has been well-documented (e.g., Jouffroy and Lessertisseur, 1960; Oxnard, 1963; Tuttle, 1969; Preuschoft, 1970; Marzke, 1971; Susman, 1979; Rose, 1988; Hunt, 1991; Stern et al., 1995; Richmond, 1998; but see Nengo, 1993). As a result, curvature serves as a useful trait in the reconstruction of posture and locomotion in fossil primates (e.g., Napier and Davis, 1959; Preuschoft, 1973a, 1974; Begun, 1993; Hamrick et al., 1995; Jungers et al., 1997; Senut et al., 2001; Nakatsukasa et al., 2003; Susman, 2004). Phalangeal curvature figures prominently in debates over whether or not early hominins, especially *Australopithecus*, had a significant arboreal component in their locomotor repertoires (Tuttle, 1981; Stern and Susman, 1983; Latimer, 1991; Susman and Stern, 1991; Nengo, 1993; Duncan et al., 1994; Gebo, 1996; Stern, 2000; Richmond, 2003).

The morphology of primate hands and feet may be particularly well-adapted to the physical properties of the substrate because of the regular direct contact that occurs with the substrate during locomotion. Substrate size, shape, and orientation have a profound influence on the biomechanical environments confronting the hands and feet as they connect the remainder of the body to the support. Most hypotheses regarding the adaptive significance of phalangeal curvature discuss potential

* Department of Anthropology, The George Washington University, 2110 G St., NW, Washington, D.C. 20052.
E-mail address: brich@gwu.edu

0047-2484/$ - see front matter © 2007 Elsevier Ltd. All rights reserved.
doi:10.1016/j.jhevol.2007.05.011

advantages of curvature in the context of grasping curved arboreal supports. Several hypotheses explicitly consider the mechanical advantages of curvature (Preuschoft, 1970, 1973b; Oxnard, 1973; Sarmiento, 1988; Hunt, 1991).

This study focuses on two hypotheses derived from the work of Preuschoft and Oxnard. Preuschoft (1970, 1973b) created theoretical biomechanical models to calculate relative bending moments and compressive and shear forces in mediolateral view in both a curved and a straight phalanx under similar mechanical conditions. Under his assumptions, the curved phalanx experienced lower bending moments than the straight phalanx, leading him to argue that "dorsal convex curvature… can be understood as an adaptation to large bending stresses" (Preuschoft, 1970: 230). This would be particularly important to climbing/suspensory primates possessing elongated phalanges that experience proportionately higher bending stresses.

Oxnard (1973: 129) similarly argued that the orangutan digit, with its highly curved phalanges, is "more efficient" than the chimpanzee digit in suspension. Using photoelastic stress models, he found that the more curved phalanx experienced lower stress, supporting Preuschoft's results based on calculated bending moments. Preuschoft (1973b) questioned the validity of Oxnard's (1973) photoelastic stress models because they lacked joints and muscle forces. Although his models were preliminary, Oxnard (1973) reached conclusions that were similar to those of Preuschoft based on a separate technique with different assumptions. Therefore, the first hypothesis predicts that phalangeal curvature reduces stress and strain during suspensory grasping.

Secondly, Preuschoft (1970, 1973b) pointed out that when fingers are flexed, the joint reaction forces are not aligned with the long axes of the phalanges. Curvature effectively aligns the bone more closely with the joint reaction force. In doing so, Preuschoft argued that the bending moments are reduced at the expense of increased compressive forces. This hypothesis leads to the prediction that more curved phalanges should experience relatively lower tension (due to decreased bending moments) and higher compression (with the addition of compressive forces to the reduced bending moments). Thus, the second hypothesis predicts that during suspensory grasping, a curved phalanx will exhibit a higher ratio of compressive to tensile strains compared to a straight phalanx.

The approaches of Preuschoft and Oxnard both involved abstract models that were unavoidably based on a variety of assumptions regarding muscle activity, anatomical geometry, and hand posture relative to the support. These factors impact the biomechanical model and the resulting stress and strain distributions (Richmond et al., 2005; Ross et al., 2005; Strait et al., 2005). This study builds upon their work by constructing a biomechanical model of suspensory grasping based on measured anatomical geometry and *in vivo* hand posture, by validating the model against cadaver strain experiments, and by testing the effects of curvature through a carefully controlled comparison. Specifically, the hypotheses that phalangeal curvature reduces strain and increases the relative amount of compression are tested here by employing finite element analysis (FEA) to compare the highly-curved manual proximal phalanx of a siamang to an artificially-straightened 'siamang' phalanx of the same length, width, and area under the same loading conditions. In this way, an attempt is made to isolate curvature and assess its mechanical consequences.

Methods

A two-dimensional (2D) model of the third manual proximal phalanx of a siamang (*Hylobates syndactylus*) was chosen to represent the mechanics of curved phalanges during suspensory grasping. Lesser apes were selected for their specialized suspensory behavior (Fleagle, 1974; Gittens, 1983), markedly curved phalanges, and availability for study. The third proximal phalanx was chosen because its central position in the hand ensures a weight-bearing role and buffers it from mediolateral forces (not modeled here). A sagittal 2D model was created because phalangeal curvature occurs in this plane and, during unimanual suspension, the predominant loading regime and bone strain occur in the sagittal plane (see Validation, below). The biomechanical measurements of the digit (see below) and proximal phalanx geometry were obtained from an adult siamang cadaver. A living siamang was not available for controlled observation, so muscle activity patterns and hand posture data were collected on a gibbon (*Hylobates lar*); therefore, this study assumes that a gibbon's hand posture and muscle recruitment during unimanual suspension is comparable to that of a siamang.

Finite element analysis

The biomechanics of phalangeal curvature were investigated using FEA, an analytical method widely used in engineering and biomechanics for the study of structural design (Beaupré and Carter, 1992; Cook et al., 2001; Richmond et al., 2005)[1]. This method involves dividing the structure of interest into a finite, but typically high, number of simple elements of defined material properties, applying loads at specific points, and calculating stress and strain for each element to obtain an approximate solution for the structure as a whole (Richmond et al., 2005). Stress (σ) is defined as force per unit area (F/A), and is a measure used to describe the internal forces in an object. Strain (ϵ) describes the deformations that result from an imposed load, and is defined as the change in length divided by original length ($\Delta L/L$) (Currey, 2002). Results are reported here in terms of strain because of its probable role in bone formation and maintenance (Rubin and Lanyon, 1985a; Biewener et al., 1986; Gross et al., 1997), and in order to facilitate comparisons with results from cadaver strain gage validation experiments. By convention, stretching a bone in tension is represented as positive strain (a positive change in length), and compression is represented as negative strain.

[1] Note that FEA is not the same method as finite element scaling analysis, which adapts FEA to the measurement of form difference between two structures in a D'Arcy Thompsonian fashion (Cheverud, 1983).

Please cite this article in press as: Brian G. Richmond, Biomechanics of phalangeal curvature, J Hum Evol (2007), doi:10.1016/j.jhevol.2007.05.011

The three fundamental steps in the FEA—model creation, solution, and validation—are described below for this study.

Biomechanical model. Developing the FE model, typically the most intensive step, involves building a biomechanical model, dividing (meshing) the structure into elements, incorporating material properties, and applying the loading conditions in an appropriate manner.

The biomechanical model (Fig. 1) was constructed with data on muscle activity, hand posture, anatomical moment arms and angles, and substrate reaction forces (SRF). These data provide estimates of the loading conditions, namely the forces acting on the proximal phalanx. Muscle recruitment was determined from electromyography (EMG) experiments on gibbons that reveal activity of the extrinsic digital flexor muscles, *flexor digitorum superficialis* (FDS) and *flexor digitorum profundus* (FDP), and inactivity of *extensor digitorum communis* (EDC) during suspension (Susman et al., 1982, and unpublished experiments by Susman and Stern). Dorsal interosseous muscles are also active (Susman and Stern, 1980), but were not modeled in this analysis as their contribution to finger flexion is thought to be minimal compared to the extrinsic flexor muscles (Preuschoft, 1973b), and the influence of interosseous muscle force (i.e., points of application and direction of force) on the phalanges is not clear during grasping.

Hand posture was modeled after a representative handhold taken from video footage of an adult male gibbon in unimanual suspension. A SONY Hi-8 video camera was placed at one end of a 1.5 inch (3.8 cm) diameter overhead support, and the hand was filmed from radioulnar view during unimanual suspension. Although it would be very interesting to sample a range of support sizes, orientations, and material properties (e.g., support flexibility), examining the influence of support variation is beyond the scope of this study. The support size (3.8 cm diameter) employed here falls within the 2 to 10 cm range of branch diameters reported to be most commonly used by gibbons while brachiating in their natural habitats (Gittens, 1983), and was the same support size used in the EMG experiments documenting muscle recruitment. Figure 1 illustrates the representative hand posture sampled here. Notice that the proximal phalanx is virtually horizontal across the top of the bar.

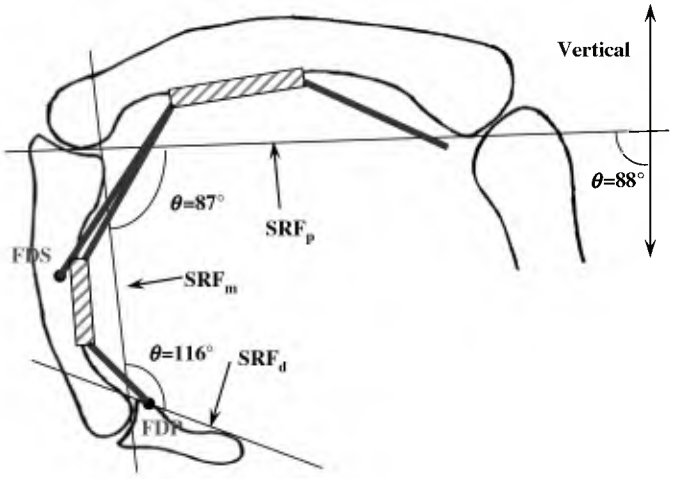

Fig. 1. Biomechanical model constructed from a videotaped and digitized hand posture of a gibbon (*Hylobates lar*) in unimanual suspension from a horizontal bar of 1.5 in. diameter, and cadaver dissection and measurement of tendon moment arms and angles. SRF = Substrate Reaction Force (d = distal phalanx; m = middle phalanx; p = proximal phalanx), FDS = *Flexor Digitorum Superficialis* tendon, FDP = *Flexor Digitorum Profundus* tendon; hatched rectangle denotes flexor sheaths; θ = angle between respective phalanges and between the proximal phalanx and vertical.

Moment arms and angles of the tendons and joint contact points on the proximal, middle, and distal phalanges were measured directly on a siamang cadaver before the bones were removed. Examples of the moment arms include the distances of the FDS insertion site and flexor sheath from the joints (Fig. 1). Using these biomechanical variables, knowledge of which muscles are active, and observed hand posture, a biomechanical model of the third digit was constructed (Fig. 1). Mean body weight for *Hylobates syndactylus* (11.05 kg) was taken from Jungers (1985), and one quarter body mass (2.76 kg) was used to calculate an estimate of the force (27 N) passing through the third digit (assuming equal distribution of body mass through digits II to V supporting the siamang's body mass). During locomotion, the body mass SRF probably does not remain equally distributed across the digits, and likely varies with speed and substrate size and orientation. The effects of these variables would be very interesting to know, but are beyond the scope of this study. For the support size and orientation in this study, an unequal distribution of SRF across digits II–V would only have an affect on the magnitude of forces and strains, but would not alter the pattern of loading and deformation, which is the focus of this study.

Five main forces act on the proximal phalanx: the substrate reaction force (SRF) from the branch, the joint reaction forces (JRF) of the metacarpal (JRF_{mc}) and middle phalanx (JRF_{mp}), and the forces of the extrinsic flexor muscles, FDS and FDP. Following a free body diagram approach (Preuschoft, 1970, 1973b), FDP and FDS forces were calculated from free body diagrams of the distal phalanx (for FDP) and middle phalanx (for FDS) with an assumption of equivalent SRFs on these phalanges. The FDP force was determined by calculating the force required to resist the torque imposed by the distal phalanx SRF (SRF_d in Fig. 1). With FDP and FDS estimates, the JRFs of the distal and proximal interphalangeal joints were calculated. Finally, the proximal phalanx SRF (SRF_p) and JRF_{mc} were calculated with a proximal phalanx free body diagram by solving the torque and translational equilibrium equations. In this manner, the five main forces were calculated and applied to the proximal phalanx model (Fig. 2c). For additional computational details, see Richmond (1998).

The tendons of FDP and FDS slide through the flexor sheath of the proximal phalanx and do not exert a force proximodistally; therefore, the combined flexor force (FD) is directed palmarly (Fig. 2d). The following are the calculated force estimates acting on the proximal phalanx (Fig. 2d): a SRF of 28.06 N directed dorsally, a joint reaction force (JRF_{mp}) from the middle phalanx of 43.85 N (θ = 61.6° from horizontal),

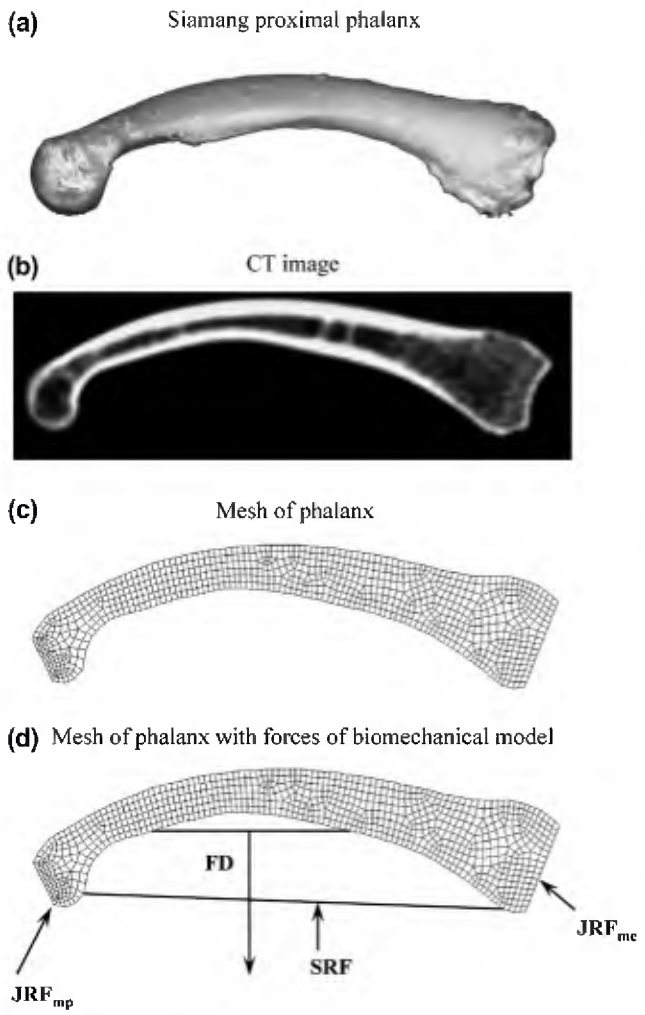

Fig. 2. a) Siamang third proximal phalanx. b) CT image of phalanx. c) Mesh constructed from the CT image and used to represent the phalanx in sagittal view. d) Mesh with the forces of the biomechanical model shown. The force vectors shown are roughly proportional to their relative magnitudes. FD is evenly distributed along the area of the flexor sheath. The SRF is evenly applied along the palmar surface of the phalanx. JRF_{mp} = joint reaction force from the middle phalanx; JRF_{mc} = joint reaction force from the metacarpal; SRF = substrate reaction force; FD = combined force of digital flexor tendons (FDS and FDP).

a JRF_{mc} from the metacarpal of 27.47 N ($\theta = -40°$ from horizontal), and 84.37 N (directed palmarly) for the force of the combined flexor musculature (FD). Because the flexor tendons lie between the substrate and proximal phalanx along its entire length (Fig. 1), the substrate does not apply a force directly on the phalanx. Instead, the flexor tendon counteracts it. Therefore, in the FE model (see below, and Fig. 4), the SRF is subtracted from the larger combined FD force.

These force estimates are not unreasonable in light of other studies. Forces as high as 80% body weight are inferred for JRFs in a single human metatarsal during normal walking (Stokes et al., 1979), compared to the highest JRF here of 40% body weight force in a siamang suspending from one hand. Changes in the body weight force have no qualitative effect on the model, but require a concomitant increase or decrease in muscle force, and thus, influence strain magnitudes but not strain distributions.

FE mesh. The siamang third proximal phalanx was CT-scanned (Fig. 2a, b), then digitized using MacMorph Image Analysis software (Spencer and Spencer, 1994). The digitized coordinates were input into the FE program ALGOR (ALGOR, Inc.) and subdivided into a mesh of linear, quadrilateral elements (Fig. 2c) using an automated mesh generator. In the absence of material property data on hylobatid phalanges, values of 18 GPa and 0.3 were taken as rough averages of the Elastic Modulus and Poisson's Ratio, respectively, for mammalian-longitudinal cortical bone samples from a number of independent studies (Currey, 2002). Although bone generally behaves anisotropically (material properties vary with orientation), data on the degree and nature (e.g., orthotropic or more complex) of anisotropy in primate phalanges are not known, nor is the variation in material properties throughout the bone (Peterson and Dechow, 2003). Furthermore, although isotropic modeling influences strain and stress magnitudes, it appears to have little effect compared to anisotropic modeling on the pattern of stress, especially in long structures subjected to bending forces (Chen and Povirk, 1996; Strait et al., 2005). Therefore, for the comparative purposes in which FEA is used here, the phalanx was treated isotropically; that is, it was assumed that mechanical properties were equivalent in all directions.

Convergence test. The mesh of small quadrilateral elements is an approximation of the original geometry of the proximal phalanx. As such, it is important to ensure that the mesh is refined enough to yield reliable estimates of stress and strain. A coarse mesh (i.e., few, large elements) may produce inaccurate estimates purely as a consequence of mesh properties. The convergence test provides a practical solution for determining appropriate mesh density. The test involves generating a number of models varying widely in mesh density, solving each model, and comparing the outcomes. In this way, the convergence test offers an empirical basis for selecting an element density high enough to yield reliable estimates (Hart, 1989).

The results of a convergence test are shown in Figure 3. Proximal phalanx FE models ranging from 18 to 2,686 nodes were created and loaded under the same conditions. The maximum principle strain at a designated node present in every model (denoted by '*' in Fig. 3) was plotted for each. At low mesh density (18 nodes, 10 elements), strain is almost half the value calculated with higher mesh densities; moreover, the strain distribution (not shown) is not smooth and differs qualitatively from more dense models. With increasing element density, strain computations rapidly converge (Fig. 3). The model with 221 nodes (176 elements) is sufficiently dense to yield reliable calculations, but near the minimum mesh density for this biomechanical model. The curved and straight models used in this paper are constructed with 963 nodes, 850 elements, and 1,025 nodes, 912 elements, respectively.

Boundary conditions. The final step in creating the FE model consists of deciding on the most appropriate application of the boundary conditions, which include loading conditions

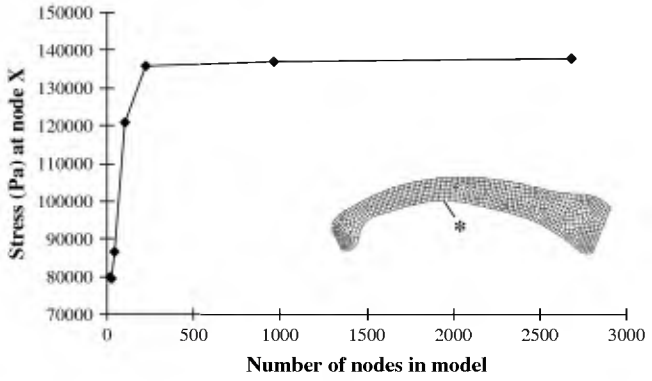

Fig. 3. Convergence test. Proximal phalanx models ranging from 18 to 2,686 nodes were created and solved, and strain at a given node was recorded for each model. The node, denoted with an asterisk (*), is the 40th node from the left along the palmar surface of the model. Results of the convergence test show that models with less than about 200 nodes do not yield precise strain values (or distributions). The model with 221 nodes (176 elements) lies along the convergence plateau and is sufficiently dense for reliable calculations. The curved and straight models used in this analysis are constructed with 963 and 1,025 nodes (850 and 912 elements), respectively.

(forces) and boundary constraints (fixed points that prevent the model from moving) (Richmond et al., 2005). The loads and boundary constraints were applied in a variety of arrangements, each consistent with the biomechanical model (Fig. 2d), to examine the sensitivity of alternative scenarios (Fig. 4). In each FE model, the main forces (FD, SRF, JRF_{mp}, JRF_{mc}) are incorporated. In the basic model, the SRF is subtracted from the larger FD force because the tendon lies palmar to the proximal phalanx and counteracts the weaker SRF. The net FD force (56.31 N) was distributed evenly along the nodes (1.52189 N/node along 37 nodes) corresponding to the flexor sheath (Fig. 4a). Instead of applying the JRFs as vectors, the node representing the proximal articular contact with the metacarpal (JRF_{mc}) is held fast from movement in either the y- or z-direction (Fig. 4). It is mathematically 'tacked down' to prevent rigid movement of the model due to slight inequalities in the biomechanical model. The distal articular node is similarly fixed in the z-direction to keep it from rotating about the fixed proximal articular node, but allowed to move in the y-direction (proximo-distal). The y-component of JRF_{mp} (from the middle phalanx; 20.8 N) was applied at the same node. In effect, the fixed nodes provide the equal and opposite reaction forces required to perfectly balance the model (see below).

The second loading scenario (Fig. 4b) simply reversed the boundary constraints, with the distal end constrained in the y- and z-directions, and the proximal end z-constrained along with the JRF_{mc} y-component. The third loading configuration (Fig. 4c) attempts to constrain the model in a manner that mimics the biological mechanism of joint restraint. Constraints are placed at the approximate positions of the interphalangeal and metacarpophalangeal collateral ligaments (Fig. 4c). Complete joint reaction forces are applied to both articular ends. The fourth model includes both y- and z-components of the JRF_{mc} and a completely fixed-based JRF_{mp} (Fig. 4d). This model resembles a cantilevered beam, following Godinot's (1991) primate phalanx model. In the fifth and final model, the SRF and FD are both applied to the nodes of the palmar bone surface to examine the effect of applying both forces to the bone surface (Fig. 4e). The SRF is directed dorsally and applied evenly along the palmar nodes (0.3225 N/node along 87 nodes). The flexor force (FD) is oriented palmarly and distributed along the nodes corresponding to the flexor sheath (−2.28 N/node along 37 nodes); the superposition of FD and SRF at these nodes results in a net −1.9575 N/node.

Solution

The FE models were solved using plane-stress quadrilateral elements. Plane stress, one of several alternatives for computing 2D solutions (in the Y-Z plane, here the parasagittal plane), sets to zero the stresses associated with the x- (mediolateral) axis (Cook et al., 2001). Although the model is 2-dimensional, it is given a uniform thickness in the x-direction of 0.0073 m, the average width of the siamang phalanx. By incorporating information on thickness, the 2D plane stress model more accurately simulated the 3D condition. All computations were performed with the FE software ALGOR on a desktop PC.

Validation

No matter how carefully one models a biomechanical problem, assumptions are unavoidable and the model may be incorrect. Therefore, the final step in a FEA attempting to accurately model a structure is the comparison of the model's behavior to independent data for validation and refinement (Huiskes and Chao, 1983; Richmond et al., 2005). For this and related studies (Richmond, 1998), a strain gage experiment was conducted using the forelimb of an adult male *Hylobates lar* cadaver (from an animal previously at the Cameron Zoo, TX, and loaned by Dr. M. Marzke). The cadaver was frozen fresh, thus avoiding the changes associated with formalin fixation to the mechanical properties of bone (Viceconti et al., 1992) and other tissues. The cadaver's joints were slightly stiffened by drying that occurred during frozen storage, but were much more mobile than available formalin-fixed specimens.

Three rosette strain gages (Tokyo Sokki Kenkyujo Co., Ltd.) were placed along the third proximal phalanx by careful dissection from a radial approach. One gage was placed on the palmar surface proximal to the flexor sheath and deep to the flexor tendons (Fig. 5). The tendons were gently pulled palmarly to expose the bone surface during the gage fixation procedure. After cutting and removing the periosteum at the gage site, the bone was degreased thoroughly with chloroform, and the gage was bonded to the surface with cyanoacrylate adhesive. The lead wires were fed to one side of the phalanx, brought proximally along the dorsum of the hand. Two gages were attached to the dorsal surface, one opposite the palmar gage, and one dorsal to the flexor sheath in the region of maximal curvature (more distally). Gage positions and orientations were recorded with images and radiographs (Fig. 5).

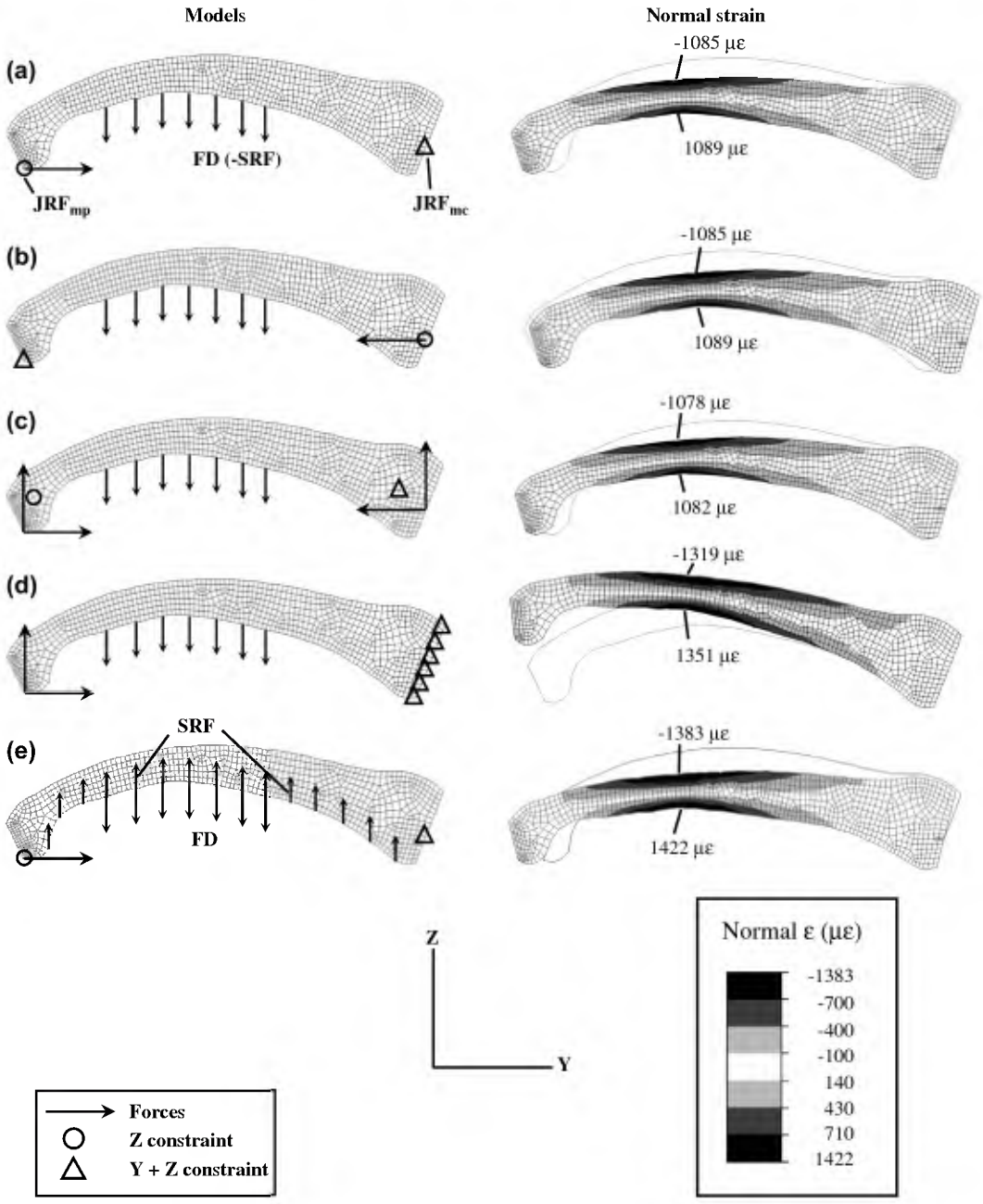

Fig. 4. Five alternative loading configurations representing the same biomechanical model are illustrated with the model (left column) and resulting normal (y-direction) strains shown on a model illustrating the deformations (right column; deformations magnified 30x to make them visible). All strains are shown to the same scale (bottom right). The normal strain values at the same dorsal and palmar nodes are also shown for each computed FE model. Note that the basic manner of deformation and pattern of strain distribution indicating dorsopalmar bending is the same in each variation of the model, with compression (negative strain) dorsally and tension (positive strain) palmarly. The basic model (a) applies the combined extrinsic flexor muscle force (FD), with the weaker and opposite substrate reaction force (SRF) subtracted from it, evenly along the nodes corresponding to the flexor sheath (1.52189 N/node along 37 nodes). The JRFs are modeled as a rigid boundary constraint at the proximal joint reaction force (JRF_{mc}) and a constraint fixed in the z-direction combined with the distal joint reaction force (JRF_{mp}) y-component (20.8 N). In (b), the JRF boundary conditions are reversed and yield identical strain patterns and magnitudes. In (c), the constraints are modeled at collateral ligament locations, and the y- and z-components of the JRFs are applied. This model's strain patterns and magnitudes are nearly identical to those of (a) and (b), illustrating how the constraints compensate for slight inequalities (rounding error, precision in load location) in balancing the free body diagram's forces. It also shows that the constraints in (a) and (b) effectively serve as reaction forces. In (d), the phalanx is modeled as a cantilevered beam, with the entire base constrained and the JRF_{mp} y- and z-components applied. Strains are considerably elevated, and extend more proximally, compared to (a–c). In (e), the first model (a) is altered such that the FD and SRF forces are both applied to the bone surface (SRF = 0.3225 N/node, 87 nodes; FD = -2.28 N/node, 37 nodes). Strains are elevated in this model and, compared to (a–c), the tension-to-compression ratio is elevated as a result of the dorsally-directed SRFs near the bone ends. Model (a) is used in subsequent analysis.

Please cite this article in press as: Brian G. Richmond, Biomechanics of phalangeal curvature, J Hum Evol (2007), doi:10.1016/j.jhevol.2007.05.011

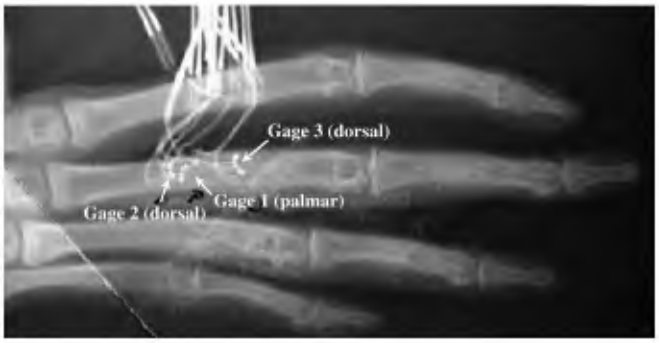

Fig. 5. Radiograph of the cadaver *H. lar* hand, in dorsal view, used in the validation study. Gage 1 is located on the palmar surface proximal to the flexor sheath, Gage 2 lies on the dorsal surface opposite Gage 1, and Gage 3 lies more distally on the dorsal surface in the region of maximum curvature.

The lead wires of the gages were soldered so that each element of a gage formed one arm of a Wheatstone bridge (Biewener, 1992; Ross and Hylander, 1996). Bridge excitation was set at 1 volt, and voltage changes were amplified using a Vishay Instruments 2100 strain gage conditioner and amplifier system, and input directly into LabView on a PC. Raw voltage values for each strain gage element were imported into IGOR Pro wave analysis software (WaveMetrics, Inc.) and converted into units of microstrain ($\mu\epsilon$) based on calibration files saved before and after each experiment. Calibrations were based on bridge excitations known to simulate $\pm$ 1,000 $\mu\epsilon$ ($\pm$ 0.1% error) at gage factor 2. Principal strain magnitudes and angle relative to element A were calculated for each rosette gage using standard trigonometric equations (Biewener, 1992). The principal strain axes are referred to the bone's long axis by adjusting for the angle between element A and the long axis, measured from radiographs. Peak maximum and minimum principal strains and the angle were recorded for each loading event of the experiments.

To simulate unimanual suspension, the gibbon forelimb was suspended from a 2 3/8″-diameter pole. A ten-pound weight attached to both FDP and FDS with a surgical clamp hung freely from the cadaver, tightening the cadaver fingers around the pole and supporting the cadaver without any additional mechanism (i.e., the cadaver hung freely from the pole when the FDP and FDS were pulled). As a cadaver experiment, true muscle forces are not known, and the purpose of the experiments is to measure strain patterns and relative magnitudes along the phalanx, rather than validate absolute strain magnitudes in the FE model. Furthermore, modeling the phalanx as a 2D structure assumes that the principal axes will approximately align with the bone's long axis. The validity of this assumption was tested with the data from multiple rosette gages.

In 2D FE models, strains may only be calculated in the sagittal plane, either along the longitudinal axis of the bone (ϵ_{11}) or dorsopalmarly (ϵ_{22}). Strains normal to the long axis predominate in the loading regimes considered here. To make cadaver strain results directly comparable to FE model results, strains normal to the long axis (normal strain, ϵ_{11}) are calculated from the cadaver experiment principal strains (Biewener, 1992).

The goal of the validation experiment is not to test whether the absolute strain magnitudes are modeled with a high degree of accuracy and precision. Creating FE models to accurately predict absolute, as well as relative, strain magnitudes would require many additional studies on the variation in anatomy, extrinsic and intrinsic hand muscle recruitment, *in vivo* kinematics and kinetics, as well as variation in material properties of bone (Richmond et al., 2005). The validation experiment performed here was designed to assess the pattern, not absolute magnitude, of loading. Therefore, there is no expectation that the FE model will match the absolute magnitudes in the strain experiment, or that the absolute magnitudes in the cadaver experiment more closely approximate those in living hylobatids than do the absolute magnitudes in the FE model. Rather, the goal is to assess whether the FE model accurately represents the pattern of deformation of the validation experiment. The compressive or tensile state of ϵ_{11} at each gage is compared with the same location on the FE model. In addition, relative tensile and compressive strains help to assess the correspondence between FE model and cadaver experiments in terms of how much global compression is combined with bending. For example, pure bending results in equal tension and compression values on either side of a beam. The addition of longitudinal compression to the beam elevates compression and reduces tension.

Curved versus straight model

In an attempt to isolate the mechanical consequences of curvature, a straight siamang phalanx of equal length and dorso-ventral width was created by mathematically rotating and translating coordinates such that the dorsal-most coordinates formed a straight line (see Fig. 8). To ensure that the areas (2D analog of mass) were equal, each model was digitized using an automated edge-detection procedure in SigmaScanPro. The areas are nearly identical: the curved (unmodified) phalanx has an area of 188.4 mm^2, and the straight model 188.5 mm^2, a difference of less than 0.07%. The straight phalanx was modeled with the same mechanical properties and subjected to identical loading conditions as in Figure 4a.

Results

Finite element model

The five alternative loading scenarios yield broadly similar results. Although care is warranted in the placement of forces and boundary conditions, the model appears to be robust with respect to subtle differences in modeling. Altering force magnitudes and directions have a much greater effect. In every model, the loads compress the dorsal surface and tense the palmar surface, with the highest strains occurring in the region of the flexor sheaths just distal to the center of the shaft (Fig. 4). The muscle and joint reaction forces strain the phalanx such that it is being 'bent open.' Recall that the JRFs are forcing the ends dorsally while the flexor tendons are pulling the central shaft palmarly in a pulley-like fashion. Although the first

Please cite this article in press as: Brian G. Richmond, Biomechanics of phalangeal curvature, J Hum Evol (2007), doi:10.1016/j.jhevol.2007.05.011

two models are displaced in an identical manner, there are slight-to-moderate differences among the other models as a result of the variation in loading conditions. For each model, an image of the amplified deformations is shown on the right of Figure 4. The differences between the five loading schemes are in magnitude and, to a lesser degree, distribution (Fig. 4, right column).

The first two arrangements (Fig. 4a, b, left column), in which the boundary constraints and the JRF y-component are reversed, produce identical results except that different ends 'move' (Fig. 4a, b, right column). Strain distribution and peak normal (y-direction) compressive and tensile strains are the same in each (−1085 με and 1089 με, respectively), demonstrating that the fixed point effectively acts as an equal and opposite reaction force to balance the model. (Note that there is only one y-directed force in both models, requiring a reaction force provided by the y- and z-fixed point).

The third loading scenario, in which the JRFs are applied and constraints mimick collateral ligament attachments, yields virtually identical strain magnitudes and patterns compared to the first two models (within 5–10 με values at the same nodes). This further illustrates the manner in which boundary constraints compensate for slight inequalities in balancing the free body diagram. These inequalities include rounding error when calculating the free body diagram, and the fact that the FE nodes may not be in precisely the same location as the force location in the free body diagram (i.e., the nodes are in discrete locations that may not precisely correspond to the free body diagram).

The fourth loading scenario (Fig. 4d), modeled after a cantilevered beam (Godinot, 1991), results in higher peak normal strain (−1319 με, 1351 με). In this model, the manner of deformation is quite different from the other models because it is not constrained on both ends as it is in life, but instead acts as a cantilevered beam. Strain is distributed farther proximally compared to the other models, as would be expected from a cantilevered beam. The fifth loading scenario behaves qualitatively like the first three models, but strains are elevated and, compared to models a–c, the tension-to-compression ratio is elevated as a result of the dorsally-directed SRFs near the bone ends (−1383 με, 1422 με). Models a–c are biologically most realistic, and match the validation results (see below), so model (a) is used in subsequent analysis.

Validation

With the proximal phalanx horizontal, maximum principal strain (E1) on the palmar surface (Gage 1) is oriented only 2.5° from the bone's long axis, therefore clearly showing that the palmar surface experiences tension along the bone's long axis (Fig. 6, Table 1). Gages 2 and 3 recorded maximum principal (tensile) strains 93° and 94° to the long axis on the dorsal surface, indicating that maximum tension occurs primarily perpendicularly to the long axis, and that compression (minimum principal strain, E2) lies along the bone's long axis (Fig. 6). The alignment of E1 on the palmar surface in combination with alignment of E2 at both gage sites on the dorsal surface testifies to a loading regime of dorsopalmar bending. Indeed, manually manipulating the cadaver proximal phalanx into dorsal concave bending resulted in very similar strain patterns (Richmond, 1998).

The cadaver strain experiment shows that principal strains lay close to the long axis of the bone, indicating that the majority of stresses and strains occur due to bending in the sagittal plane. Since dorsoventral bending appears to be the dominant deformation regime, the sagittal plane provides the best 2D representation of the mechanical environment, and the use of 2D FE models is justified.

Figure 7 compares the strains calculated by the FE model to those measured by the cadaver strain experiment. The FE ϵ_{11} values are in good overall agreement with the cadaver strain data. In the FE model, the palmar surface experiences tensile strains, matching the cadaver strain results in that tensile strains are consistently observed at the palmar gage (Gage 1). Likewise, the dorsal surface experiences high compressive strains in both the FE model and the cadaver strain experiment (Table 1 and Fig. 7). Not only do the FE and experimental results agree in showing compression dorsally and tension palmarly, the *relative* magnitudes of compression and tension compare well. In both the FE model and the cadaver experiment, strains at the dorsal Gage 3 site (FE: −1186 με; gage: −447 με) are roughly twice the magnitude of the strains at the palmar Gage 1 site (FE: 663 με; gage: 218 με). Strains at the more proximal dorsal Gage 2 location are compressive in both the FE and cadaver experiment, but the magnitude is relatively lower in the FE model compared to the experiment. This suggests that the dorsal strain may be concentrated slightly distally in the FE model compared to the cadaver

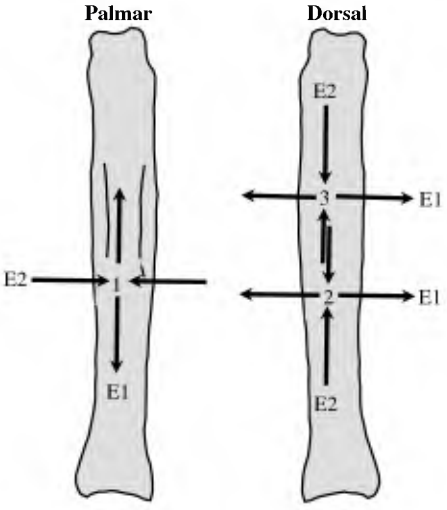

Fig. 6. Maximum (E1; tension) and minimum (E2; compression) principal strain orientations are shown at three gage locations on the third manual proximal phalanx of a gibbon cadaver during suspension, with proximal phalanx roughly horizontal. Note that the palmar surface (left) experienced tension along the shaft, and the dorsal surface (right) experiences compression, validating the FE model prediction that the proximal phalanx is bent dorsally concave during unimanual suspension. These results also indicate that a 2D sagittal view captures the principal deformations during suspensory grasping. Arrows not to scale.

Table 1
Maximum (E1) and minimum (E2) principal strains (με), orientation (Θ_{E1}, in degrees) of E1 to bone's longitudinal axis, and normal strain along (Nε1) and transverse to (Nε2), the long axis of the gibbon proximal phalanx during the cadaver strain experiment

Gage 1 (palmar)					Gage 2 (dorsal, proximal)					Gage 3 (dorsal, distal)				
E1	E2	Θ_{E1}	Nε1	Nε2	E1	E2	Θ_{E1}	Nε1	Nε2	E1	E2	Θ_{E1}	Nε1	Nε2
220	−75.5	2.5	218	−74	203	−472	−93.5	−469	200	180	−451	−94.5	−447	176

experiment. This relatively subtle discrepancy is probably due to slight differences in the anatomy between the siamang finger used to build the FE model and the gibbon used for the cadaver experiment, and other biomechanical variables.

As mentioned in the methods, the goal of the validation experiment is not to test the validity of the absolute strain magnitudes in the FE model. Despite this, the magnitudes of strain are comparable to strains recorded *in vivo* on primate long bones (e.g., Demes et al., 1998). The goal of the validation study is to assess whether the FE model accurately represents the pattern of deformation (e.g., manner of bending, compression, etc.) during one-handed suspension, as tested against the cadaver strain experiment. In this regard, the cadaver strain experiment shows good correspondence with the FE model and validates the FE result that the proximal phalanx is bent in a dorsally concave manner.

Straight versus curved models

Of the various loading scenarios tested in the curved model (Fig. 4), the first loading scenario was applied to the straight siamang phalanx model for strain comparisons (Fig. 8). As in the curved models, the straight model is bent with compression dorsally and tension palmarly, and the strain distribution is broadly similar to that of the curved model (Fig. 8). However, the magnitude of strain at comparable locations in the straight model is over twice that of the curved model (Figs. 8, 9). This difference is attributable to curvature because area, forces, and boundary conditions are virtually identical in the two models, lending strong support to Oxnard's (1973) and Preuschoft's (1970, 1973b) hypothesis that curved phalanges undergo less stress. Furthermore, the curved model consistently experiences lower strains compared to the straight model subjected to the other four loading scenarios (not shown).

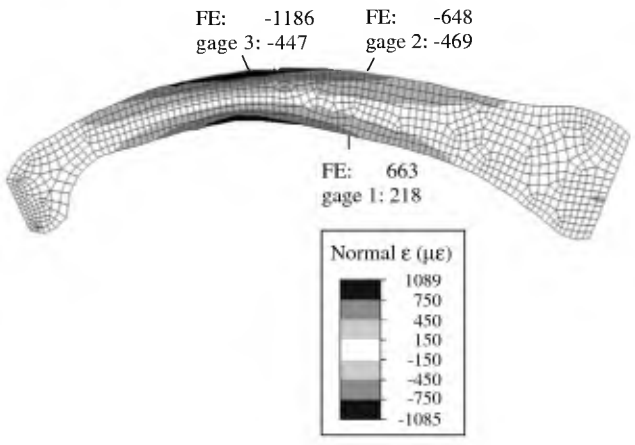

Fig. 7. FE model illustrating normal strain (in με) along the longitudinal axis (ε11). ε11 magnitudes calculated in the FE model and measured with strain gages are shown at the three gage sites. Note that both the FE model and strain results show that the palmar surface experiences tension and the dorsal surface compression.

The hypothesis that curvature transforms bending into compression is partly supported here. The ratio of peak normal compressive to tensile strain is 83.7% in the straight model and 97.6% in the curved model, indicating a relative increase in compression (due to a disproportionate decrease in tension) in the curved model (Figs. 8, 9). Respective ratios of about 84% and 95% are observed in other loading scenarios as well. When sampling beyond the peak strain nodes, compressive strains exceed tensile strains along most of the shaft. Although compressive strains are relatively higher in the curved model, dorso-palmar bending is the predominant effect in both models.

Discussion

The FE and *in vitro* strain experiment results show that the dominant mechanical regime of the proximal phalanx during suspensory grasping postures is dorsally concave bending coupled with compression, confirming previous theoretical work (Preuschoft, 1973b). During grasping with flexed joints, the proximal phalanx behaves like a beam being bent 'open.' This interpretation is also supported by the distribution of cortical bone, which is relatively thick (see Fig. 2b) in the region of greatest normal strain (Figs. 2, 7), and the orientation of collagen fibers in siamang proximal phalanges (Doden, 1993).

Both hypotheses examined in this study are supported by the results: bone strain is lower in curved phalanges (Oxnard, 1973), and bending is reduced along with a relative increase in compression (Preuschoft, 1970, 1973b). The curved phalanx model experiences roughly half the normal strain and exhibits a higher compression-to-tension ratio compared to the straight phalanx despite identical mechanical properties, equivalent areas, and forces and constraints at comparable nodes.

Mechanism of strain reduction

So, how does curvature reduce strain in a suspensory, gripping posture? At least two mechanisms are plausible. First, the positions of forces and nodes are not precisely identical in the curved and straight models. Although the models are nearly identical size (length and area), the JRFs at the centers of the joint surfaces in the curved model are 'tucked in,' facing slightly palmarly, and also slightly (about 7%) closer to the midshaft (compare the curved and straight models in Fig. 8).

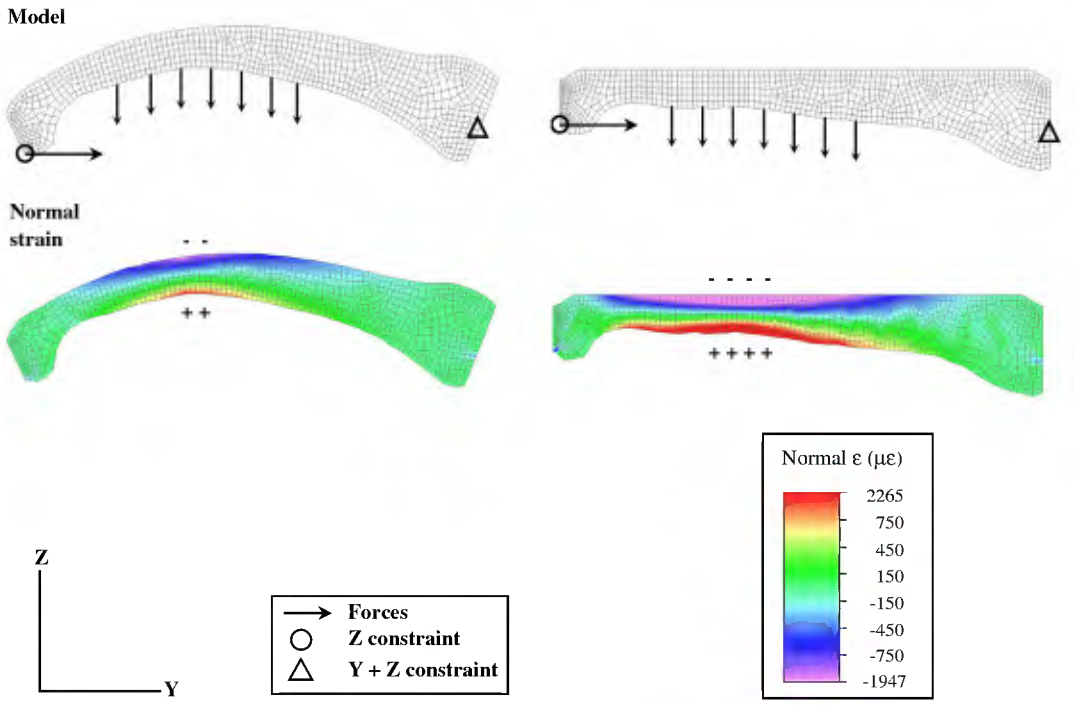

Fig. 8. The model of the curved (normal) siamang proximal phalanx is shown on the left, with the mathematically straightened rendition of equal length, width, and area to the right. Forces and boundary conditions are applied at the same nodes. Normal strains (compression and tension in the proximo-distal, or y-direction) in the straight model are over twice those in the curved model; the images are shown at the same strain scale (scale at lower right).

This slightly reduces the moment arms between the JRFs and FD. A straight model with the JRFs placed at the same spatial coordinates (vs. same node) yields about 10% lower peak normal strains. This decrease is responsible for roughly 20% of the difference between the curved and straight model, leaving about 80% of the difference unexplained. Curved phalanges are typically found in primates with long fingers that increase the compass of the hand (Susman, 1979). Although it is plausible that curvature may act as a mechanism to help reduce the long moment arm between the joints and the powerful flexor tendons, this mechanism can only account for a fraction of the strain reduction resulting from longitudinal curvature.

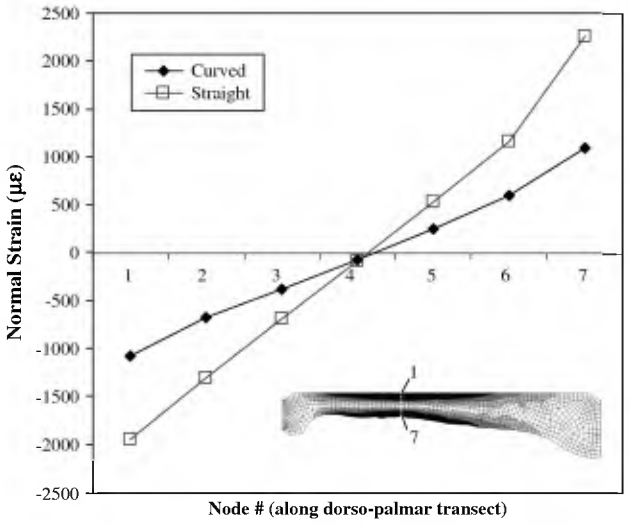

Fig. 9. Strain distribution across a dorso-palmar transect (shown at bottom right on the straight model) of nodes in the region of maximum strain. Notice that compressive and tensile strains are lower in the curved model, despite having the same length and area. The peak compression-to-tension strain ratio is somewhat higher in the curved model, indicating that curvature reduces strain and disproportionately reduces tensile strain.

The second mechanism is one proposed by Preuschoft (1970, 1973b). Greater curvature aligns the bone shaft more closely with the JRF during a gripping hand posture. When curved phalanges assume a flexed finger posture, the proximo-distal component (y-directed) of the JRF bends the phalanx palmarly concave ('curve closing'), and thereby effectively counteracts the palmarly convex ('curve opening') bending regime imposed by the powerful FD (Fig. 10). The ability of the JRF and FD bending regimes to counteract each other is dependent on these forces' moment arms, where the FD moment arm is the length to the flexor sheath and the y-JRF moment arm is the 'height' of the midshaft or the magnitude of curvature. In other words, the greater the curvature, the greater is the moment arm for the JRF to resist the tendency of the flexor muscle force to bend open the phalanx when the fingers are flexed (Fig. 10).

The effect of this 'force alignment' mechanism is supported by the observation that peak normal strains nearly double (1.67, 1.85 times greater at the palmar and dorsal peak strains, respectively) when the proximo-distal component of the JRF (20.8564 N) is *removed* from the model. In the straight model, removal of the y-JRF increases strain by a much more modest 1.14–1.2 times. This modest increase occurs because the

Please cite this article in press as: Brian G. Richmond, Biomechanics of phalangeal curvature, J Hum Evol (2007), doi:10.1016/j.jhevol.2007.05.011

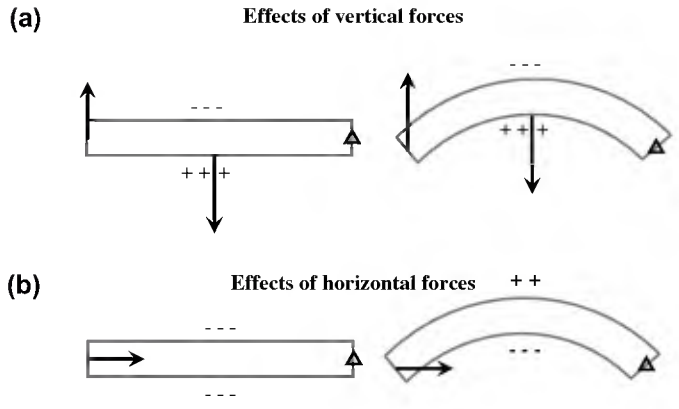

Fig. 10. Vertical forces (a) cause both straight (left) and curved (right) beams to bend similarly, in a dorsally concave manner, with compression on top and tension on bottom (the curved beam would experience less tension because the bone axis is partly aligned with the vertical force). Horizontal forces (b), however, affect the straight and curved beam differently. These forces compress the straight beam (left), whereas they bend the curved beam in a palmarly concave manner that counteracts the vertical forces in (a). In this way, curved phalanges reduce strain when joint reaction forces are oriented dorsally, such as when the fingers are flexed when suspending from and climbing relatively small supports.

y-JRF is applied palmarly enough in the straight model to have a slight 'curvature' effect.

The force alignment can also explain the higher compression-to-tension ratio in the curved phalanx. The strain reduction due to curvature is proportional to the z-axis (dorsopalmar) moment arm between the JRF and FD nodes. A longer vertical moment arm (i.e., greater curvature) increases the 'closing' bending moment of the JRF, thereby more effectively resisting the 'opening' bending moment of the FD and reducing strain magnitudes in the curved model (Fig. 10). The compressive component of the JRF is added to those reduced bending strains, resulting in a higher compression-to-tension ratio observed in the curved phalanx. As the bone shaft becomes more closely aligned with the JRF, the JRF results in greater compression and less bending of the shaft. Therefore, greater curvature reduces strain, and results in lower bending and more longitudinal compression, in flexed joint postures. This supports Preuschoft's (1970, 1973b) argument, and provides an explanation for the results presented here, that relative compressive forces increase while bending forces decrease.

The proximal phalanx offers an interesting comparison in the discussion regarding long bone curvature in general. Although the proximal phalanx shares similar length and width proportions with appendicular long bones, it appears to be loaded very differently than most long bones (e.g., Biewener, 1983; Gross et al., 1992). *In vivo* data show that curvature in weight-bearing long bones accentuates, rather than minimizes, bone strain (Lanyon and Baggott, 1976; Rubin and Lanyon, 1982; Biewener et al., 1983; Rubin, 1984; Biewener and Taylor, 1986). Over 80% of measured strain in the femur, humerus, radius, ulna, and tibia is caused by bending moments (Rubin et al., 1990). These observations led some to hypothesize that long bone curvature exists in order to make strains more predictable because curvature has the effect of channeling the manner in which bones deform over a range of loading conditions (Lanyon and Rubin, 1985; Bertram and Biewener, 1988; Rubin et al., 1990). The curved proximal phalanx appears to be an unusual case in that bending occurs in the opposite direction of curvature, and offers no apparent improvement in strain predictability.

In addition to these observations, the strain distribution along a dorsopalmar cross-section is fairly linear (Fig. 9). Thus, it appears that siamang phalanges are not curved or, especially, are not dorso-palmarly thick enough to elicit the nonlinear bending strains of curved beams (Timoshenko, 1958), such as that observed in the mandibular symphysis (Hylander, 1985).

If curvature reduces strain so effectively, then why do many primates have relatively straight phalanges? Curvature's ability to reduce strain in the manner described above only holds true for flexed joint postures (Preuschoft, 1973b). In unflexed joint postures, curvature would cause the phalangeal shaft to be poorly aligned with the JRFs and have a quite different strain distribution (Richmond, 1998). Indeed, it would be very interesting to examine the interaction between support size, grip posture, and the resulting strain distribution. The results of this and related studies (Preuschoft, 1973b; Richmond, 1998) suggest that the degree of finger flexion (at both the metacarpophalangeal [MP] and proximal interphalangeal [PIP] joints) is the primary factor in determining the pattern (not magnitude) of strain distribution. For example, smaller diameter supports require greater flexion, whereas large diameter supports require less flexion. When primates suspend from very small supports relative to their size, they often place their PIP joints along the top of the support with a highly flexed PIP joint, and typically an unflexed MP joint. In this case, the advantages of curvature would be more relevant to the distal end of the shaft, and I would hypothesize that the biomechanics of such postures are partly responsible for the typically distal concentration of curvature along the phalangeal shaft.

Strain distributions and bone modeling

The interaction between degree of finger flexion during locomotion and strain distribution throughout the phalangeal shaft may help explain observed changes in curvature during ontogeny. For example, gorillas practice less arboreality and more terrestriality as they grow to adulthood (Doran, 1997). Data suggest there is an *increase* in curvature from birth to young juvenile age as they begin practicing the greatest amount of arboreal behavior (Richmond, 1998, 2003; Jungers et al., 2001). After this age, both the degree of arboreality and phalangeal curvature decrease significantly towards adulthood. This pattern is also observed in chimpanzees (Paciulli, 1995). These results suggest either that curvature is such a strongly-controlled adaptive trait that it is tightly linked to behaviors practiced at different times during growth, or that curvature is partly a modeling response to functional behavior during growth. Either case indicates a strong functional link.

Please cite this article in press as: Brian G. Richmond, Biomechanics of phalangeal curvature, J Hum Evol (2007), doi:10.1016/j.jhevol.2007.05.011

This pattern of diaphyseal growth is consistent with experimental data demonstrating the critical role of functional activity for the development of curvature. For example, the rat tibia develops normal length but does not develop normal curvature in the absence of normal functional activity (Lanyon, 1980). *In vivo* strain data during growth in chicks shows that the pattern of bone strain magnitude, sign (i.e., compression, tension), and orientation remain unchanged during growth, even over 10-fold increases in bone mass and three-fold increases in bone length (Biewener et al., 1986). Biewener et al. (1986: 393) note that "the state of strain within and along the bone's length likely represents an important stimulus for adjustments in bone mass and shape during postnatal growth." These data and others (e.g., Rubin and Lanyon, 1985b; Robling et al., 2006) suggest that the biomechanical consequences of using the hands and feet in arboreal and terrestrial settings influence phalangeal development.

Conclusion

In conclusion, the strain differences between curved and straight phalanges illustrated here support the common assertion that phalangeal shaft curvature is related to the strains associated with arboreal and especially suspensory activity (e.g., Oxnard, 1973; Preuschoft, 1973b; Susman, 1979; Tuttle, 1981; Rose, 1988; Sarmiento, 1988; Stern et al., 1995; Richmond, 1998), and may underlie changes in curvature during ontogeny in response to changes in mechanical environments of arboreal and terrestrial supports (Richmond, 1998, 2003).

Acknowledgements

Thanks to Jack Stern, Jr. and Randy Susman for access to unpublished EMG experiments. Thanks also to Mary Marzke who kindly loaned her cadaver gibbon forelimb, Clint Rubin for the loan of strain gage instrumentation, Callum Ross for help with the strain data analyses, and Y.-X. Qin for discussions about FE modeling. Thanks also to Bill Jungers, Brigitte Demes, Adam Gordon, Janine Chalk, David Green, Nicole Griffin, Susan Antón, the Associate Editor, and three anonymous reviewers for helpful comments. This research was supported by NSF SBR-9624726, NSF BCS-0240865, NSF BCS-9806291, and the DPAS.

References

Beaupré, G.S., Carter, D.S., 1992. Finite element analysis in biomechanics. In: Biewener, A.A. (Ed.), Biomechanics-Structures and Systems: A Practical Approach. IRL Press at Oxford University Press, Oxford, pp. 149–174.

Begun, D.R., 1993. New catarrhine phalanges from Rudabanya (Northeastern Hungary) and the problem of parallelism and convergence in the hominoid postcranial morphology. J. Hum. Evol. 24, 373–402.

Bertram, J.E.A., Biewener, A.A., 1988. Bone curvature: sacrificing strength for load predictability? J. Theor. Biol. 131, 75–92.

Biewener, A.A., 1983. Locomotor stresses in the limb bones of two small animals: the ground squirrel and chipmunk. J. Exp. Biol. 103, 131–154.

Biewener, A.A., 1992. *In vivo* measurement of bone strain and tendon force. In: Biewener, A.A. (Ed.), Biomechanics–A Practical Approach. Oxford University Press, Oxford, pp. 123–148.

Biewener, A.A., Swartz, S.M., Bertram, J.E.A., 1986. Bone modeling during growth: dynamic strain equilibrium in the chick tibiotarsus. Calcif. Tissue Int. 39, 390–395.

Biewener, A.A., Taylor, C.R., 1986. Bone strain: a determinant of gait or speed? J. Exp. Biol. 123, 383–400.

Biewener, A.A., Thomason, J., Goodship, A.E., Lanyon, L.E., 1983. Bone stresses in the horse forelimb during locomotion at different gaits: a comparison of two experimental methods. J. Biomech. 16, 565–576.

Chen, X., Povirk, G., 1996. Assessing errors introduced by modeling the anisotropic human mandible isotropically with finite element method. Am. J. Phys. Anthropol. 22 (Suppl.), 83.

Cheverud, J., Lewis, J.L., Bachrach, W., Lew, W.D., 1983. The measurement of form and variation in form: an application of three-dimensional quantitative morphology by finite-element methods. Am. J. Phys. Anthropol. 62, 151–165.

Cook, R.D., Malkus, D.S., Plesha, M.E., Witt, R.J., 2001. Concepts and Applications of Finite Element Analysis. John Wiley & Sons, New York.

Currey, J.D., 2002. Bones: Structures and Mechanics. Princeton University Press, Princeton.

Demes, B., Stern Jr., J.T., Hausman, M.R., Larson, S.G., McLeod, K.J., Rubin, C.T., 1998. Patterns of strain in the macaque ulna during functional activity. Am. J. Phys. Anthropol. 106, 87–100.

Doden, E., 1993. The relationship between the function and inner cortical structure of metacarpal and phalangeal bones. In: Preuschoft, H., Chivers, D.J. (Eds.), Hands of Primates. Springer-Verlag, Wien, pp. 271–284.

Doran, D.M., 1997. Ontogeny of locomotion in mountain gorillas and chimpanzees. J. Hum. Evol. 32, 323–344.

Duncan, A.S., Kappelman, J., Shapiro, L., 1994. Metatarsophalangeal joint function and positional behavior in *Australopithecus afarensis*. Am. J. Phys. Anthropol. 93, 67–81.

Fleagle, J.G., 1974. Dynamics of a brachiating siamang [*Hylobates (Symphalangus) syndactylus*]. Nature 248, 259–260.

Gebo, D.L., 1996. Climbing, brachiation, and terrestrial quadrupedalism: historical precursors of hominid bipedalism. Am. J. Phys. Anthropol. 101, 55–92.

Gittens, S.P., 1983. Use of the forest canopy by the agile gibbon. Folia Primatol. 40, 134–144.

Godinot, M., 1991. Approches functionnelles des main de primates paleogenes. Geobios 13, 161–173.

Gross, T.S., Edwards, J.L., McLeod, K.J., Rubin, C.T., 1997. Strain gradients correlate with sites of periosteal bone formation. J. Bone Miner. Res. 12, 982–988.

Gross, T.S., McLeod, K.J., Rubin, C.T., 1992. Characterizing bone strain distributions *in vivo* using three triple rosette strain gages. J. Biomech. 25, 1081–1087.

Hamrick, M.W., Meldrum, D.J., Simons, E.L., 1995. Anthropoid phalanges from the Oligocene of Egypt. J. Hum. Evol. 28, 121–145.

Hart, R.T., 1989. The finite element method. In: Cowin, S.C. (Ed.), Bone Mechanics. CRC Press, Boca Raton, pp. 53–74.

Huiskes, R., Chao, E.Y.S., 1983. A survey of finite element analysis in orthopedic biomechanics: the first decade. J. Biomech. 16, 385–409.

Hunt, K.D., 1991. Mechanical implications of chimpanzee positional behavior. Am. J. Phys. Anthropol. 86, 521–536.

Hylander, W.L., 1985. Mandibular function and biomechanical stress and scaling. Am. Zool. 25, 315–330.

Jouffroy, F.K., Lessertisseur, J., 1960. Les specialisations anatomiques de la main chez les Singes a progression suspendue. Mammalia 24, 93–151.

Jungers, W.L., 1985. Body size and scaling of limb proportions in primates. In: Jungers, W.L. (Ed.), Size and Scaling in Primate Biology. Plenum, New York, pp. 345–381.

Jungers, W.L., Godfrey, L.R., Simons, E.L., Chatrath, P.S., 1997. Phalangeal curvature and positional behavior in extinct sloth lemurs (Primates, Paleopropithecidae). Proc. Natl. Acad. Sci. U. S. A. 94, 11998–12001.

Jungers, W.L., Godfrey, L.R., Simons, E.L., Wunderlich, R.E., Richmond, B.G., Chatrath, P.S., Rakotosamimanana, B., 2001.

Ecomorphology and behavior of giant extinct lemurs from Madagascar. In: Plavcan, J.M., Kay, R.F., Van Schaik, C.P., Jungers, W.L. (Eds.), Reconstructing Behavior in the Primate Fossil Record. Kluwer Academic/Plenum Publishers, New York, pp. 371–411.

Lanyon, L.E., 1980. The influence of function on the development of bone curvature: an experimental study on the rat tibia. J. Zool. (Lond.) 192, 457–466.

Lanyon, L.E., Baggott, D.G., 1976. Mechanical function as an influence on the structure and form of bone. J. Bone Joint Surg. 58B, 436–443.

Lanyon, L.E., Rubin, C.T., 1985. Functional adaptation in skeletal structures. In: Hildebrand, M., Bramble, D.M., Liem, K.F., Wake, D.B. (Eds.), Functional Vertebrate Morphology. Belknap Press, Cambridge, MA, pp. 1–25.

Latimer, B.M., 1991. Locomotor adaptations in *Australopithecus afarensis*: the issue of arboreality. In: Coppens, Y., Senut, B. (Eds.), Origine(s) de la Bipédie chez les Hominidés. CNRS, Paris, pp. 169–176.

Marzke, M.W., 1971. Origin of the human hand. Am. J. Phys. Anthropol. 34, 61–84.

Nakatsukasa, M., Kunimatsu, Y., Nakano, Y., Takano, T., Ishida, H., 2003. Comparative and functional anatomy of phalanges in *Nacholapithecus kerioi*, a Middle Miocene hominoid from northern Kenya. Primates 44, 371–412.

Napier, J.R., Davis, P.R., 1959. The forelimb skeleton and associated remains of *Proconsul africanus*. Foss. Mamm. Afr. 16, 1–70.

Nengo, I.O., 1993. Integrating mechanical and historical approaches to organismal design: the case of shaft structure in the hands and feet of Catarrhines. Ph.D. Dissertation, Harvard University.

Oxnard, C.E., 1963. Locomotor adaptations in the primate forelimb. Symp. Zool. Soc. Lond. No. 10 (the Primates), 165–182.

Oxnard, C.E., 1973. Form and Pattern in Human Evolution: Some Mathematical, Physical, and Engineering Approaches. University Chicago Press, Chicago.

Paciulli, L.M., 1995. Ontogeny of phalangeal curvature and positional behavior in chimpanzees. Am. J. Phys. Anthropol. 20 (Suppl.), 165.

Peterson, J., Dechow, P.C., 2003. Material properties of the human cranial vault and zygoma. Anat. Rec. 274A, 785–797.

Preuschoft, H., 1970. Functional anatomy of the lower extremity. In: Bourne, G.H. (Ed.), The Chimpanzee, vol. 3. Karger, Basel, pp. 221–294.

Preuschoft, H., 1973a. Body posture and locomotion in some east African Miocene Dryopithecinae. In: Day, M.H. (Ed.), Human Evolution (Symposium of the Society for the Study of Human Biology, Volume XI). Taylor and Francis, London, pp. 13–46.

Preuschoft, H., 1973b. Functional anatomy of the upper extremity. In: Bourne, G.H. (Ed.), The Chimpanzee, vol. 6. Karger, Basel, pp. 34–120.

Preuschoft, H., 1974. Body posture and mode of locomotion in fossil primates – method and example: *Aegyptopithecus zeuxis*. Symp. 5th Cong. Int. Primatol. Soc. 345–359.

Richmond, B.G., 1998. Ontogeny and biomechanics of phalangeal form in primates. Ph.D. Dissertation, State University of New York at Stony Brook, Stony Brook.

Richmond, B.G., 2003. Early hominin locomotion and the ontogeny of phalangeal curvature in primates. Am. J. Phys. Anthropol. 36 (Suppl.), 178–179.

Richmond, B.G., Wright, B.W., Grosse, I., Dechow, P.C., Ross, C.F., Spencer, M.A., Strait, D.S., 2005. Finite element analysis in functional morphology. Anat. Rec. A Discov. Mol. Cell Evol. Biol. 283, 259–274.

Robling, A.G., Castillo, A.B., Turner, C.H., 2006. Biomechanical and molecular regulation of bone remodeling. Annu. Rev. Biomed. Eng. 8, 455–498.

Rose, M.D., 1988. Functional anatomy of the cheiridia. In: Schwartz, J. (Ed.), Orang-utan Biology. Oxford University Press, Oxford, pp. 299–309.

Ross, C.F., Hylander, W.L., 1996. *In vivo* and *in vitro* bone strain in the owl monkey circumorbital region and the function of the postorbital septum. Am. J. Phys. Anthropol. 101, 183–215.

Ross, C.F., Patel, B.A., Slice, D.E., Strait, D.S., Dechow, P.C., Richmond, B.G., Spencer, M.A., 2005. Modeling masticatory muscle force in finite element analysis: sensitivity analysis using principal coordinates analysis. Anat. Rec. A Discov. Mol. Cell Evol. Biol. 283, 288–299.

Rubin, C.T., 1984. Skeletal strain and the functional significance of bone architecture. Calcif. Tissue Int. 36, 11–18.

Rubin, C.T., Lanyon, L.E., 1982. Limb mechanics as a function of speed and gait: a study of functional strains in the radius and tibia of horse and dog. J. Exp. Biol. 101, 187–211.

Rubin, C.T., Lanyon, L.E., 1985a. Regulation of bone formation by applied dynamic loads. J. Bone Joint Surg. (Am.) 66-A, 308–314.

Rubin, C.T., Lanyon, L.E., 1985b. Regulation of bone mass by mechanical strain magnitude. Calcif. Tissue Int. 37, 411–417.

Rubin, C.T., McLeod, K.J., Bain, S.D., 1990. Functional strains and cortical bone adaptation: epigenetic assurance of skeletal integrity. J. Biomech. 23, 43–54.

Sarmiento, E.E., 1988. Anatomy of the hominoid wrist joint: its evolutionary and functional implications. Int. J. Primatol. 9, 281–345.

Senut, B., Pickford, M., Gommery, D., Mein, P., Cheboi, K., Coppens, Y., 2001. First hominid from the Miocene (Lukeino Formation, Kenya). Comp. Rend. Acad. Sci. 332 (série IIa), 137–144.

Spencer, M.A., Spencer, G.S., 1994. MacMorph Image Analysis Software. Stony Brook, NY.

Stern Jr., J.T., 2000. Climbing to the top: a personal memoir of *Australopithecus afarensis*. Evol. Anthropol. 9, 113–133.

Stern Jr., J.T., Jungers, W.L., Susman, R.L., 1995. Quantifying phalangeal curvature: an empirical comparison of alternative methods. Am. J. Phys. Anthropol. 97, 1–10.

Stern Jr., J.T., Susman, R.L., 1983. The locomotor anatomy of *Australopithecus afarensis*. Am. J. Phys. Anthropol. 60, 279–317.

Stokes, I.A.F., Hutton, W.C., Stott, J.R.R., 1979. Forces acting on the metatarsals during normal walking. J. Anat. 129, 579–590.

Strait, D.S., Wang, Q., Dechow, P.C., Ross, C.F., Richmond, B.G., Spencer, M.A., Patel, B.A., 2005. Modeling elastic properties in finite-element analysis: how much precision is needed to produce an accurate model? Anat. Rec. A Discov. Mol. Cell Evol. Biol. 283, 275–287.

Susman, R.L., 1979. Comparative and functional morphology of hominoid fingers. Am. J. Phys. Anthropol. 50, 215–235.

Susman, R.L., 2004. *Oreopithecus bambolii*: an unlikely case of hominidlike grip capability in a Miocene ape. J. Hum. Evol. 46, 103–115.

Susman, R.L., Jungers, W.L., Stern Jr., J.T., 1982. The functional morphology of the accessory interosseous muscle in the gibbon hand: determination of locomotor and manipulatory compromises. J. Anat. 134, 111–120.

Susman, R.L., Stern Jr., J.T., 1980. EMG of the interosseous and lumbrical muscles in the chimpanzee (*Pan troglodytes*) hand during locomotion. Am. J. Anat. 157, 389–397.

Susman, R.L., Stern Jr., J.T., 1991. Locomotor behavior of early hominids: epistemology and fossil evidence. In: Coppens, Y., Senut, B. (Eds.), Origine(s) de la Bipédie Chez les Hominidés. Centre National de la Recherche Scientifique, Paris, pp. 121–131.

Timoshenko, S., 1958. Strength of Materials - Part 1: Elementary Theory and Problems. D. Van Nostrand Co., New York.

Tuttle, R.H., 1969. Quantitative and functional studies on the hands of the anthropoidea: I. The Hominoidea. J. Morphol. 128, 309–363.

Tuttle, R.H., 1981. Evolution of hominid bipedalism and prehensile capabilities. Phil. Trans. R. Soc. Lond. B292, 89–94.

Viceconti, M., Toni, A., Giunti, A., 1992. Strain gauge measurements of hard tissues: factors influencing measurements. In: Little, E.G. (Ed.), Experimental Mechanics: Technology Transfer between High Tech Engineering and Biomechanics. Elsevier Science Publishers, London, pp. 177–184.

Please cite this article in press as: Brian G. Richmond, Biomechanics of phalangeal curvature, J Hum Evol (2007), doi:10.1016/j.jhevol.2007.05.011